JCTC Journal of Chemical Theory and Computation

Article

pubs.acs.org/JCTC

Probing a Continuous Polar Defect: A Reaction Coordinate for Pore Formation in Lipid Membranes

Jochen S. Hub* and Neha Awasthi

Institute for Microbiology and Genetics, University of Göttingen, Justus-von-Liebig Weg 11, 37077 Goettingen, Germany

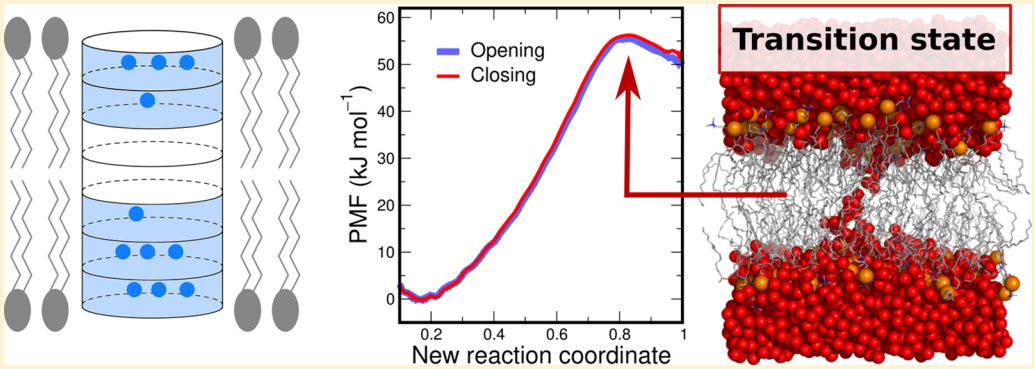

ABSTRACT: Various biophysical processes involve the formation of aqueous pores over lipid membranes, including processes of membrane fusion, antimicrobial peptide activity, lipid flip-flop, and membrane permeation. Reliable and efficient free-energy calculations of pore formation using molecular dynamics simulations remained challenging due to the lack of good reaction coordinates (RCs) for pore formation. We present a new RC for pore formation that probes the formation and rupture of a continuous polar defect over the membrane. Potential of mean force (PMF) calculations along the new RC rapidly converge and exhibit no hysteresis between pore-opening and pore-closing pathways, in contrast to calculations based on previous RCs. We show that restraints along the new RC may restrain the system tightly to the transition state of pore formation, rationalizing the absence of hysteresis. We observe that the PMF of pore formation in a tension-free membrane of dimyristoylphosphatidylcholine (DMPC) reveals a free-energy barrier for pore nucleation, confirming a long-hypothesized metastable prepore state. We test the influence of the lipid force field, the cutoff distance used for Lennard-Jones interactions, and the lateral membrane size on the free energies of pore formation. In contrast to PMF calculations based on previous RCs, we find that such parameters have a relatively small influence on the free energies of pore nucleation. However, the metastability of the open pore in DMPC may depend on such parameters. The RC has been implemented into an extension of the GROMACS simulation software. The new RC allows for reliable and computationally efficient free-energy calculations of pore formation in lipid membranes.

INTRODUCTION

The formation of polar defects in lipid membranes plays an important role in various biophysical processes. Antimicrobial peptides act via formation of aqueous pores in membranes.[1] During membrane fusion, the hemifused state progresses to the fusion pore via the formation of a polar defect.[2,3] Pore formation provides a mechanism for programmed cell death triggered by the immune response.[4] In addition, membrane electroporation is an established method for transferring various types of material across membranes, such as RNA and vaccines, with applications in cell biology and medicine.[5,6]

Over the last years, molecular dynamics (MD) simulations have provided detailed mechanistic insight into pore formation. Pores were induced in silico by applying surface tension[7,8] or electric fields,[6,9,10] by enforcing lipid flip-flop,[11−14] by steering the lipids laterally from the defect,[15−17] or by pulling water[18] or ions into the membrane.[19] Pores are believed to form first by the penetration of a thin water needle into the membrane, followed by tilting of lipids parallel to the membrane to avoid unfavorable contacts of water with the apolar membrane interior.[6,7,13]

The free energy landscape of pore formation, however, has remained controversial. Nearly 40 years ago, Abidor et al. hypothesized the existence of a metastable prepore state,[20] stabilized because closing of a pore requires to reorient the tilted lipids back to an upright position. Under membrane tension, Zhelev and Needham reported long-lived large pores with a radius of ∼1 μm,[21−23] stabilized by nonequilibrium solvent flow through the pore.[24] Computationally, metastable pores were reported from simulations of stretched membranes.[25] In tension-free membranes, in contrast, a pore nucleation barrier, as required to rationalize a metastable pore, was not resolved in the potential of mean force (PMF) of pore formation.[16,26] This finding is in contrast to recent reports of long-lived pores in simulations of a dimyristoylphosphatidylcholine (DMPC) membrane.[26] Apart from such discussions

Received: February 1, 2017
Published: April 4, 2017

DOI: 10.1021/acs.jctc.7b00106
J. Chem. Theory Comput. 2017, 13, 2352−2366

on pore formation in pure-lipid systems, calculations on the effect of membrane-active compounds, such as antimicrobial peptides, on the free energies of pore formation have remained difficult.[27] Such uncertainties are partly a consequence of the lack of good reaction coordinates for pore formation, as discussed in the following.

PMF calculations are a standard method for obtaining the energetics along functionally relevant transitions in biomolecular systems, such as pore formation in membranes. PMF calculations require the definition of one or multiple reaction coordinates (or order parameters), yet identifying good reaction coordinates (RCs) for complex transitions is often far from trivial.[28,29] However, problems may arise when using unsuitable RCs, as illustrated in Figure 1. A hypothetical free energy landscape is shown as contour lines in Figure 1A, exhibiting two valleys, named state A and state B, respectively, connected by a saddle point (or transition state, TS). Similar landscapes have been discussed before.[28,30] The minimum free energy path (MFEP) connecting states A and B (Figure 1A, red arrow) leads over the transition state and reveals a free energy barrier separating states A and B (Figure 1B, red curve). From a good RC one would expect: (i) The PMF along the RC should at least resemble the MFEP and exhibit the free energy barrier. (ii) Under nonequilibrium conditions, upon slowly pulling the system along a good RC from state A to state B or back from state B to state A, the system should more or less follow the MFEP. Here, "slow" refers to time scales accessible in an MD simulation. Properties i and ii would be fulfilled if restraints applied along the RC are capable of restraining the system close to the transition state.

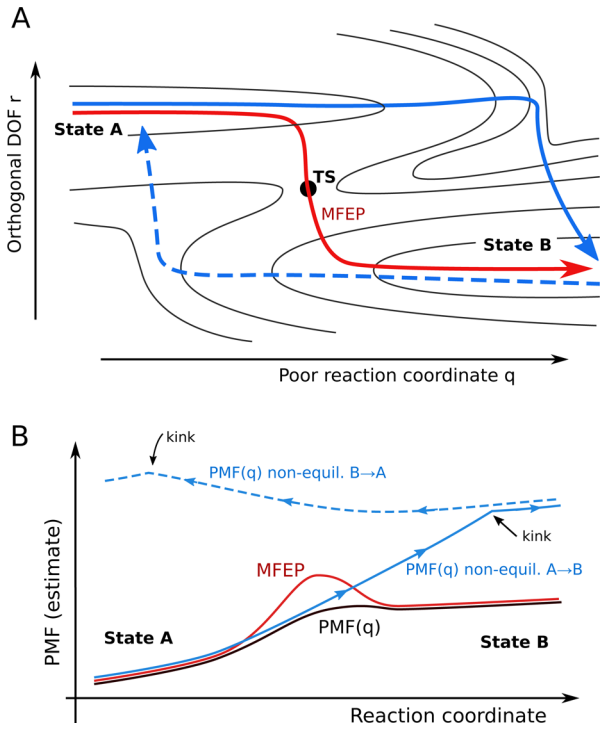

Figure 1. (A) Hypothetical two-valley energy landscape, illustrating two possible problems with poor reaction coordinates (RCs). The minimum free energy path (MFEP, red arrow), passing over the transition state (TS), would reveal a free energy barrier separating states A and B (red line in panel B, bottom). In contrast, the PMF along a poor reaction coordinate (A, horizontal black arrow) would not reveal the barrier, since the barrier would be integrated out along the orthogonal degree of freedom (DOF), leading to a "hidden barrier" (black line in panel B). In addition, upon pulling the system along the poor RC within finite simulation time, sampling problems may lead to hysteresis (blue arrows in panel A) and incorrect estimates for the free energy difference between states A and B (blue lines in panel B). For a more detailed explanation, see text.

When using a poor reaction coordinate as indicated by the black horizontal arrow in Figure 1A, the desirable properties i and ii may be violated. First, if the barrier is crossed orthogonal to the RC in phase space, the barrier is integrated out upon computing the PMF (Figure 1B, black curve). Hence, the PMF would not reveal that state B is metastable. In the context of membrane simulations, related problems have been discussed in detail by Neale and co-workers, who referred to such integrated out barriers as "hidden barriers".[31,32] Yet a second more practical problem may arise as a consequence of finite simulation time: upon pulling the system under nonequilibrium conditions along the poor RC, the system might not properly sample states A and B. For instance, starting in state A, the system may miss the transition state and instead be pulled up the valley of state A to states of increasing free energy, until the system eventually falls into state B (Figure 1A, blue solid arrow). Hence, the system may be perturbed more strongly than strictly required to reach state B. The PMF estimated from such simulations may overestimate the free energy difference between states A and B. The position at which the system falls into state B appears as a kink in the PMF estimate (Figure 1B, blue solid curve). In turn, upon pulling the system back to state A along the poor RC, the system may take a different pathway, i.e., hysteresis may appear (Figure 1A, blue broken arrow). The system may be pulled up the valley of state B to large free energies, until the system eventually falls into state A. The PMFs estimated from the forward and backward pulling simulations would strongly differ (Figure 1B, blue solid and broken lines). Critically, the true free energy difference between states A and B may take any value between the estimates from the forward and backward nonequilibrium pulling simulations. Although, here we argued in the light of nonequilibrium pulling, hysteresis may persist in umbrella sampling or constrained simulations along such poor RCs, since the initial coordinates for umbrella and constrained windows are typically taken from a nonequilibrium pulling simulation conducted either in forward or backward direction. How severe the problems with hidden barriers and hysteresis are in practice depends on the free energy landscape, the barriers involved, the chosen RC, and the degree of sampling (or simulation time).

Since methods for computing the MFEP, such as the string method,[33] are computationally expensive for biomolecular systems, there are no simple solutions for circumventing the problems described above, yet some methods for detecting hidden barriers have been discussed.[32] As a simple measure to test for hidden barriers, free simulations can be started in the state of higher free energy, corresponding to state B in Figure 1. Rapid transitions down to state A or metastability of state B may give indications on a free energy barrier. To test for hysteresis, the PMF can be computed from simulation frames taken from nonequilibrium pulling simulations conducted in forward and backward direction. If the PMFs from forward and backward pulling do not agree, indicative of hysteresis, caution in the interpretation of the PMFs is advised.

In a recent study,[26] we systematically compared three different reaction coordinates that have been used for PMF calculations of transmembrane pore formation. (a) The

DOI: 10.1021/acs.jctc.7b00106
J. Chem. Theory Comput. 2017, 13, 2352−2366

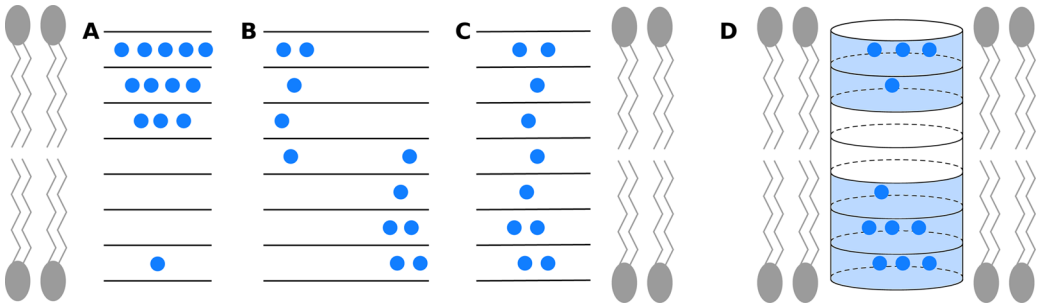

Figure 2. (A–C) Illustration of common aqueous defects in a lipid membrane: (A) asymmetric "hanging droplet" structure, (B) two laterally displaced partial water defects, and (C) continuous defects spanning the complete membrane. The reaction coordinate (RC) proposed here is capable of differentiating between these three common structures. (D) Illustration of the proposed reaction RC, defined via a membrane-spanning cylinder that is decomposed into "slices" along the membrane normal (illustration, 7 slices). The RC ξ is given by the fraction of slices that are occupied by polar atoms, as indicated by blue shaded surfaces (illustration, $\xi \approx 5/7$).

distance d_{ph} of a single lipid phosphorus atom from the membrane center, corresponding to a lipid flip-flop process.[11−14] This RC is similar to the coordinate used for pulling ions or small peptides into a membrane.[19,34−36] (b) The collective RC by Tolpekina et al.,[15−17] that guides the lipids laterally from the defect axis. (c) The RC by Mirjalili and Feig[18] given by the average water density inside a membrane-spanning cylinder. Pulling systems along these three RCs efficiently introduced pores into the membranes. However, PMF calculations revealed problems that may be rationalized by the energy landscape in Figure 1. First, PMFs along none of the RCs revealed a nucleation barrier in a membrane of 128 DMPC lipids modeled with the Berger force field,[37] despite the fact that the open pore was stable for 10 μs of simulation, suggesting that a barrier was integrated out.[26] In addition, we observed pronounced hysteresis between pore-opening and pore-closing pathways. For instance, during umbrella sampling simulations along the water density coordinate,[18] 500 ns of sampling per umbrella window was required to remove hysteresis. With the lipid flip-flop coordinate,[11] even 1 μs per umbrella window did not remove hysteresis. Moreover, the free energy of pore formation computed with the RC by Tolpekina et al.[15] was larger as compared to results using the other RCs, suggesting that the membrane was more strongly perturbed than strictly required for pore formation. These problems prompted us to develop an alternative RC, which is introduced in the present article.

This Article is organized as follows. First, a new RC is introduced, designed to probe the presence or absence of a continuous polar defect over the membrane. We show that PMF calculations using umbrella sampling along the new RC rapidly converge and are not affected by hysteresis. We explicitly demonstrate that restraints applied along the new RC restrain the system close to the transition state of pore formation. The influence of free parameters required to define the RC is carefully analyzed, leading to reasonable default settings of such free parameters. Finally, we investigate the role of lipid force fields, membrane system size, and cutoff settings for Lennard-Jones interactions on the PMFs of pore formation.

THEORY

Reaction Coordinate for Probing a Continuous Polar Defect. The RC is designed to differentiate between (i) polar defects partly penetrating the membrane (Figure 2A/B) and (ii) a continuous defect spanning the entire membrane (Figure 2C). To this end, we defined the RC using a membrane-spanning cylinder that is decomposed into N_s slices along the membrane normal (Figure 2D). The thickness d_s of the slices is chosen such that pairs of polar atoms in neighboring slices are capable of forming stable hydrogen bonds, even in the presence of some disorder and fluctuations. A reasonable value of the parameter d_s is 1 Å. The slices are taken symmetrically around the center of mass Z_{mem} of the hydrophobic membrane atoms along the membrane normal. Hence, the center of slice s is given by $z_s = Z_{mem} + \left(s + \frac{1}{2} - N_s/2\right)d_s$, where $s = 0, ..., N_s - 1$.

The RC is defined as the fraction of slices that are occupied by polar heavy atoms:

$$\xi = N_s^{-1} \sum_{s=0}^{N_s-1} \delta_s(N_s^{(p)}) \tag{1}$$

Here, $N_s^{(p)}$ denotes the number of polar heavy atoms within slice s of the membrane-spanning cylinder. As polar atoms contributing to $N_s^{(p)}$, we used water oxygen atoms as well as the four oxygen atoms of the lipid phosphate groups. The symbol δ_s is a continuous indicator function ($0 \le \delta_s < 1$), which equals zero if no polar atom is located in slice s ($N_s^{(p)} = 0$) and takes a value close to unity if one or multiple polar atoms are located in the slice ($N_s^{(p)} \ge 1$). Importantly, δ_s remains smaller than unity, irrespective of how many polar atoms are located in slice s. This property is crucial in order to distinguish between the cases of (i) few slices occupied by many polar atoms, as present in a geometry of a hanging droplet (Figure 2A), and (ii) every slice occupied by at least one polar atom, as present in a continuous polar defect (Figure 2C).

To carry out umbrella sampling in an MD simulation along the RC, ξ must be differentiable with respect to the coordinates of the atoms. Hence, we formulate δ_s and $N_s^{(p)}$ as differentiable switch functions as follows:

$$\delta_s(N_s^{(p)}) = \psi(N_s^{(p)}; \zeta) \tag{2}$$

where ψ denotes the switch function

$$\psi(x; \zeta) = \begin{cases} \zeta x & \text{if } x \le 1 \\ 1 - ce^{-bx} & \text{if } x > 1 \end{cases} \tag{3}$$

The parameter ζ indicates the fraction to which a slice is filled upon the addition of the first polar atom into the slice. A typical value for ζ would be 0.75. The parameters b and c are taken as $b = \zeta/(1 - \zeta)$ and $c = (1 - \zeta)e^b$, leading to the continuous and differentiable switch function shown in Figure 3A. Importantly,

DOI: 10.1021/acs.jctc.7b00106
J. Chem. Theory Comput. 2017, 13, 2352−2366

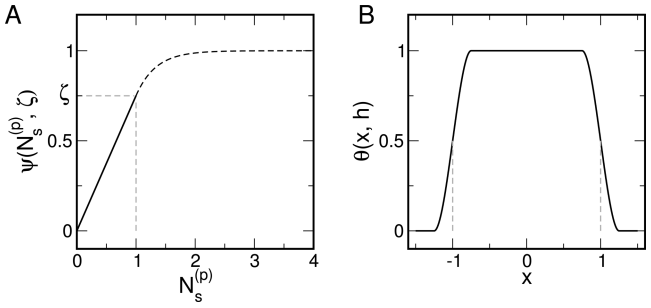

Figure 3. Switch functions used to define a reaction coordinate that is differentiable with respect to the positions of the atoms. (A) Switch function $\psi(N_s^{(p)}; \zeta)$, indicating whether a slice is occupied or not. The parameter ζ determines the fraction to which the slice is filled upon the addition of the first atom. A reasonable value is $\zeta = 0.75$. (B) Continuous step function $\theta(x,h)$ used to define if an atom is located within a slice or not. $2h$ is the width of the switch region. We used $h = 1/4$.

since $\psi(N_s^{(p)}, \zeta)$ rapidly saturates at $N_s^{(p)} > 1$, the RC ξ is strongly increased by the addition of the first polar atom to any slice, and ξ is only marginally increased by the addition of a second or third polar atom to the same slice. Hence, the function ψ indeed approximates an indicator function for "occupied" slices. Likewise, the number of polar atoms $N_s^{(p)}$ located in slice s is formulated in terms of switch functions as follows:

$$N_s^{(p)} = \sum_{i=1}^{N^{(p)}} f(\mathbf{r}_i, z_s, d_s, X_{\mathrm{cyl}}, Y_{\mathrm{cyl}}, R_{\mathrm{cyl}}) \tag{4}$$

Here, $\mathbf{r}_i = (x_i, y_i, z_i)$ are the Cartesian coordinates of atom i, and $N^{(p)}$ is the number of polar heavy atoms in the entire system, here taken as the oxygen atoms of water and lipid phosphate groups. The indicator function f takes unity if atom i is located within slice s *and* within a cylinder of radius R_{cyl} around the polar defect, and it takes zero otherwise. The coordinates $(X_{\mathrm{cyl}}, Y_{\mathrm{cyl}})$ denote the lateral position of the cylinder axis, located approximately at the polar defect (see below). A typical value for the cylinder radius R_{cyl} is 1.2 nm. Defining the RC with such a cylinder-shaped indicator functions is required to distinguish between (i) two laterally displaced partial defects in each membrane leaflet (Figure 2B), which may be stabilized by membrane undulations, and (ii) a single continuous defect over the entire membrane (Figure 2C).

Similar to Mirjalili and Feig,[18] we decompose the indicator function f into a radial and an axial contribution

$$f = f_{\mathrm{axial}}(z_i, z_s, d_s) f_{\mathrm{radial}}(x_i, y_i, X_{\mathrm{cyl}}, Y_{\mathrm{cyl}}, R_{\mathrm{cyl}}) \tag{5}$$

The radial and axial indicator functions are formulated as differentiable functions using the following step function $\theta(x;h)$ based on third-order polynomials, where $2h$ is the width of the switch region (Figure 3B):[18]

$$\theta(x; h) = \begin{cases} 1 & \text{if } -1 + h \le x \le 1 - h \\ \frac{1}{2} - \frac{3}{4h}(x-1) + \frac{1}{4h^3}(x-1)^3 & \text{if } 1 - h < x < 1 + h \\ \frac{1}{2} + \frac{3}{4h}(x+1) - \frac{1}{4h^3}(x+1)^3 & \text{if } -1 - h < x < -1 + h \\ 0 & \text{otherwise} \end{cases} \tag{6}$$

In this work, we used $h = 1/4$. The axial and the radial indicator functions were defined as

$$f_{\mathrm{axial}}(z_i, z_s, d_s) = \theta\left(\frac{z - z_s}{d_s/2}; h\right) \tag{7}$$

$$f_{\mathrm{radial}}(x_i, y_i, X_{\mathrm{cyl}}, Y_{\mathrm{cyl}}, R_{\mathrm{cyl}}) = \theta\left(\frac{r_i}{R_{\mathrm{cyl}}}; h\right) \tag{8}$$

where $r_i = [(x_i - X_{\mathrm{cyl}})^2 + (y_i - Y_{\mathrm{cyl}})^2]^{1/2}$ denotes the lateral distance of atom i from the cylinder axis. Notably, upon moving an atom from a singly occupied slice into a neighboring empty slice, the RC remains constant. This useful property holds because (a) $\theta(x; h)$ is symmetric around the inflection points at ± 1 and (b) $\psi(x; \zeta)$ is linear up to $x = 1$ (Figure 3A and B).

Lateral and Normal Center of the Defect. The RC outlined in the previous paragraph requires (a) the definition for the lateral center of the defect $(X_{\mathrm{cyl}}, Y_{\mathrm{cyl}})$, around which the cylinder is aligned, as well as, (b) the center of the membrane along the membrane normal Z_{mem}, used to define the position of the slices. The latter was simply taken as the center of mass of the heavy lipid-tail atoms,

$$Z_{\mathrm{mem}} = N_{\mathrm{a}}^{-1} \sum_{j=1}^{N_{\mathrm{a}}} z_j \tag{9}$$

where N_{a} denotes the number of lipid tail atoms. Defining the slice positions relative to the Z_{mem} ensures that the RC does change if the membrane drifts in z direction during the simulation.

Defining the lateral center of mass is more involved because we simulate with periodic boundary conditions. In a longer simulation, the defect may drift laterally over the periodic boundaries, which cannot be prevented by simple measures such as a common center of mass motion removal of a group of atoms. Consequently, the defect may become broken over the periodic boundaries, leading to problems when using standard center of mass calculations. Therefore, we used a center of mass definition that remains valid in systems with periodic boundary condition.[38,39] This can be achieved by mapping the x and y coordinates of the atoms onto the unit circle and, subsequently, averaging the sine and cosine of the angle.

In the following, we describe the definition of the x coordinate of the cylinder center X_{cyl}. The y coordinate Y_{cyl} is defined analogously. For a careful introduction into the center of mass definition used here we refer to the appendix of ref 39. The Cartesian coordinate x_i of atom i is mapped onto the unit circle using $\theta_i^x = 2\pi x_i / L_x$, where L_x is the box dimension in x direction. Subsequently, the sine and the cosine of θ_i^x are averaged over the atoms with appropriately chosen weights as follows:

DOI: 10.1021/acs.jctc.7b00106
J. Chem. Theory Comput. 2017, 13, 2352−2366

Table 1. Summary of Umbrella Sampling PMF Calculations Conducted for This Study[a]

lipid/water force field	N_{lip}[b]	t (ns)[c]	ζ	R_{cyl} (nm)	d_s (nm)	r_{LJ} (nm)[d]	Figure[a]
Berger/SPC	128	140	0.75	0.8	0.1	1.0	4B; 6A, B; 8A, B, C; 11A
Berger/SPC	128	50	0.65	0.8	0.1	1.0	8A, B, C
Berger/SPC	128	50	0.85	0.8	0.1	1.0	8A
Berger/SPC	128	50	0.75	0.6	0.1	1.0	8B
Berger/SPC	128	50	0.75	1.2	0.1	1.0	8B
Berger/SPC	128	50	0.75	1.6	0.1	1.0	8B
Berger/SPC	128	50	0.75	∞	0.1	1.0	8B
Berger/SPC	128	50	0.75	0.8	0.07	1.0	8C
Berger/SPC	128	50	0.75	0.8	0.15	1.0	8C
Berger/SPC	128	50	0.75	0.8	0.2	1.0	8C
Slipids/TIP3P	128	50	0.75	0.8	0.1	1.2	11A
CHARMM36/TIPS3P[e]	128	50	0.75	0.8	0.1	1.2[f]	11A
Berger/SPC	64	100	0.75	0.8	0.1	1.0	12
Berger/SPC	96	60	0.75	0.8	0.1	1.0	12
Berger/SPC	162	60	0.75	0.8	0.1	1.0	12
Berger/SPC	128	100	0.75	0.8	0.1	0.9	13A
Berger/SPC	128	100	0.75	0.8	0.1	1.2	13A
Berger/SPC	128	50	0.75	0.8	0.1	1.4	13A
Berger DPPC/SPC	128	100	0.75	0.8	0.1	0.9	13B
Berger DPPC/SPC	128	100	0.75	0.8	0.1	1.0	13B
Berger DPPC/SPC	128	100	0.75	0.8	0.1	1.2	13B
Berger DPPC/SPC	128	60	0.75	0.8	0.1	1.4	13B

[a]The lipids were DMPC if not stated otherwise. [b]Number of lipids. [c]Simulation time per umbrella window. [d]cutoff for Lennard-Jones potentials. [e]CHARMM-modified TIP3P. [f]Switched potential, see Methods.

$$\begin{pmatrix} X_{cyl}^{sin} \\ X_{cyl}^{cos} \end{pmatrix} = \sum_{s=0}^{N_s-1} \frac{w_s^{(cyl)}}{W} \sum_{i=1}^{N^{(p)}} \frac{f_{axial}(z_i, z_s, d_s)}{F_s} \begin{pmatrix} \sin(\theta_i^x) \\ \cos(\theta_i^x) \end{pmatrix} \tag{10}$$

where we introduced the normalization constants $W := \sum_{s=0}^{N_s-1} w_s^{(cyl)}$ and $F_s := \sum_{i=1}^{N^{(p)}} f_{axial}(z_i, z_s, d_s)$. Accordingly to eq 10, the $\sin(\theta_i^x)$ and $\cos(\theta_i^x)$ are first averaged over the atoms in each slice s, as given by the sum over $N^{(p)}$ atoms weighted by the indicator function $f_{axial}(z_i, z_s, d_s)$. Subsequently, a weighted sum over all slices is conducted, as given by the sum over s. The weight $w_s^{(cyl)}$ for slice s was taken as

$$w_s^{(cyl)} = \tanh F_s \tag{11}$$

Hence, the weights $w_s^{(cyl)}$ are close to unity if the slice is occupied by an atom, irrespective of whether the atom is within the cylinder or not. In addition, the weights $w_s^{(cyl)}$ never exceed one, even if the slice is occupied by many atoms. This definition ensures that the cylinder center (X_{cyl}, Y_{cyl}) is dominated by the atoms in the thin polar defect, but not by the large number of polar atoms in the headgroup or bulk water region. Finally, the center of mass of the cylinder is defined by mapping back the averages in eq 10 into the interval $[0, L_x]$ of the Cartesian coordinate

$$X_{cyl} = [\text{atan } 2(-X_{cyl}^{sin}, X_{cyl}^{cos}) + \pi]\frac{L_x}{2\pi} \tag{12}$$

where the function atan2(y,x) denotes the two-parameter inverse tangent function implemented in many computer programming languages.

The derivatives of the RC with respect to the atomic positions, as required to compute the atomic forces, are evaluated in the Appendix. The RC was implemented into an in-house version of Gromacs 4.6,[40] that is available from the authors upon request.

METHODS

Simulation Setup and Parameters. Membrane systems of 64, 96, 128, or 162 DMPC lipids and 40 water molecules per lipid were build with the MemGen web server.[41] If not stated otherwise, results for the 128-lipid system are reported below. The simulation setup and parameters were identical to our previous study.[26] Accordingly, the system was equilibrated until the box dimensions and the potential energy were fully converged. If not stated otherwise, parameters from Berger et al.[37] were used for DMPC and water was modeled with the SPC model.[42] The simulations were performed with the GROMACS 4.6 software.[40] Bonds and angles of water were constrained with the SETTLE algorithm,[43] and all other bonds were constrained with LINCS.[44] The temperature of the simulations was controlled at 323 K, if not stated otherwise, using a stochastic dynamics integrator.[45] The pressure was controlled at 1 bar using a semi-isotropic weak coupling scheme (τ = 1 ps).[46] Electrostatic interactions were calculated using the particle-mesh Ewald method.[47,48] Dispersion interactions and short-range repulsion were described by a Lennard-Jones (LJ) potential, which was cut off at 1 nm, if not stated otherwise. The direct-space Coulomb cutoff was set to the same value as the LJ cutoff distance. Since the DMPC model does not contain any explicit hydrogen atoms, a time step of 4 fs was applied.

To test the influence of the force field, additional simulations were conducted using the Slipids force field with with TIP3P water model,[49,50] as well as using the CHARMM36 force field with the CHARMM-modified TIP3P model (with LJ interactions on hydrogen atoms).[51] During CHARMM36 simulations, only the chemical bonds involving hydrogen atoms were constrained. A switched LJ potential was used with cutoff at 1.0 and 1.2 nm, and the direct-space Coulomb interactions were truncated at at 1.2 nm. During Slipid simulations, LJ as well as direct-space Coulomb interactions

DOI: 10.1021/acs.jctc.7b00106
J. Chem. Theory Comput. 2017, 13, 2352−2366

were truncated at 1.2 nm. A time step of 2 fs was applied. All other parameters were identical to the Berger simulations.

Umbrella Sampling and PMF Calculation. PMFs were computed along the reaction coordinate ξ (eq 1) using the technique of umbrella sampling.[52] Starting frames for umbrella sampling were either taken from a "slow-growth" pore-opening or, to exclude that the PMFs are affected by hysteresis, from a pore-closing simulation. Accordingly, starting in the equilibrium state, the pore was opened by pulling the system along ξ with a harmonic potential (force constant 3000 kJ mol^{-1}). The minimum of the harmonic potential was moved with constant velocity from $\xi = 0$ at time 0 to $\xi = 1$ at 50 ns. Subsequently, the system was restrained at $\xi = 1$ for 100 ns to equilibrate the fully open pore. Eventually, the system was pulled back to $\xi = 0$ within another 50 ns. PMFs in Figure 6B were computed from initial frames taken from the pore-closing simulation, all other PMFs were computed from the initial frames taken from the pore-opening simulation.

Umbrella sampling was performed using 24 umbrella windows. To ensure that the transition state of pore formation is well sampled, we used tighter spacing of umbrella windows and larger force constants at at $\xi \geq 0.7$ as compared to $\xi < 0.7$. Accordingly, 11 windows were distributed between $\xi = 0$ and $\xi = 0.65$ in steps of 0.065, using a force constant of 5000 kJ mol^{-1}. Additional 13 windows were distributed between $\xi = 0.7$ and $\xi = 1$ in steps of 0.025, using a force constant of 10 000 kJ mol^{-1}. Each umbrella window was simulated between 50 and 140 ns (Table 1). The first 10 ns were omitted for equilibration, if not stated otherwise. The PMFs were constructed from the umbrella histograms with the weighted histogram analysis method (WHAM), as implemented in the g_wham software.[53,54]

Parameters for the New Reaction Coordinate. If not stated otherwise, the following parameters were used during PMF calculations: N_s= 26, d_s = 0.1 nm, R_{cyl} = 0.8 nm, and ζ = 0.75. To test the influence of d_s, additional simulations using the following sets of N_s/d_s were used: 13/0.2, 17/0.15, and 37/0.07 nm. To test the influence of R_{cyl}, additional simulations were conducted using values of R_{cyl} of 0.6, 1.2, 1.6, and infinite. To test the influence of ζ, additional simulations were conducted using ζ = 0.65 and ζ = 0.85. The parameters used for all PMFs computed for this study are summarized in Table 1.

Maximum-Likelihood Estimates for the Lifetime of the Open Pore. As shown in the Results section, we used free simulations starting from the open pore to test the metastability of the open pore. The lifetime τ of the open pore was estimated from M free simulations of simulation time T_s. Let m denote the number of simulations in which the pore closed within simulation time T_s, such that the pore was still open at time T_s in $(M - m)$ simulations. Let t_i $(i = 1, ..., m)$ denote the simulation times of the closing transitions, where $0 \leq t_i \leq T_s$. Assuming a simple monoexponential decay to the closed state, the probability that the pore is still open at time t is given by $\exp(-t/\tau)$, where t is the simulation time. Hence, the probability for observing a closing event at t_i is proportional to $\exp(-t_i/\tau)/\tau$, and the probability that a pore closes at any time after T_s is given by $\exp(-T_s/\tau)$. Hence, a likelihood L for observing m pore closure events at times t_i, while observing $(M - m)$ open pores at time T_s can be formulated, as $L \propto [\prod_{i=1}^{m} \exp(-t_i/\tau)/\tau] \times [\exp(-T_s/\tau)]^{(M-m)}$. Maximizing $\log(L)$ yields the maximum-likelihood estimate for the pore lifetime $\tau_{ml} = m^{-1}[(M - m)\ T_s + \sum_{i=1}^{m} t_i]$. As expected, if the pore closed in all M simulations $(m = M)$, then τ_{ml} reduces to the common mean lifetime following $\tau_{ml}\ (m = M) = M^{-1} \sum_{i=1}^{M} t_i$.

RESULTS AND DISCUSSION

PMF of Pore Formation in DMPC Exhibits a Nucleation Barrier. We used umbrella sampling to compute the PMF for pore formation in a membrane of 128 DMPC lipids (see Methods), using 140 ns of simulation time per umbrella window. All PMFs were computed in the NPT ensemble at a constant pressure of 1 bar and in absence of any applied surface tension. The umbrella histograms in Figure 4A exhibit sufficient overlap along the reaction coordinate (RC). Notably, the histograms are not Gaussian but instead exhibit some equidistant spikes. These spikes may be rationalized by the fact that integer occupancies of the slices $(N_s^{(p)} = 1, 2, ...)$ are more likely than fractional occupancies. Consequently, positions along ξ that are realized purely by integer occupancies have slightly increased free energy or, equivalently, exhibit spikes in the umbrella histograms. Hence, the spikes do not imply poor convergence but merely reflect variations of entropy as a consequence of the coarseness of the RC.

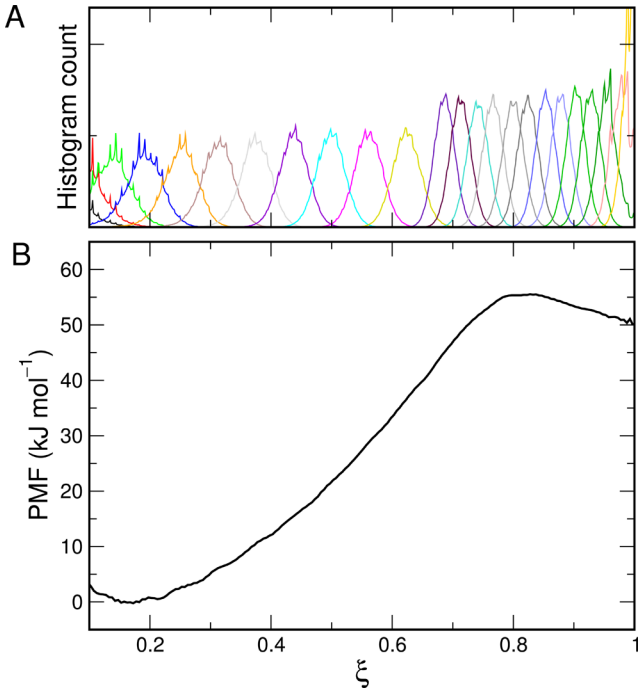

Figure 4. (A) Umbrella histograms and (B) PMF for pore formation in a DMPC membrane on the basis of 140 ns simulation time per umbrella window. The PMF exhibits a clear nucleation barrier at ξ = 0.8, implying metastability of the open pore ($\xi \approx 1$). The spikes in the umbrella histograms reflect the coarseness of the reaction coordinate, that is, integer occupancies of slices are more likely than fractional occupancies.

Figure 4B presents the PMF for pore formation, where $\xi \approx 0.2$ corresponds to the flat intact membrane, $\xi \approx 1$ to the fully formed open pore, and $\xi \approx 0.8$ to the transition state of pore formation. The free energy of the open pore of ~50 kJ mol^{-1} is in reasonable agreement with previous PMF calculations of a similar simulation system but using different RCs. Indeed, PMF calculations using the position of a single phosphorus atom with respect to the membrane center d_{ph} as RC suggested free energies of pore formation between 45 and 55 kJ mol^{-1} (refs 13

DOI: 10.1021/acs.jctc.7b00106
J. Chem. Theory Comput. 2017, 13, 2352−2366

and 26). PMF calculations based on the water density coordinate by Mirjalili and Feig[18] suggested 55 kJ mol^{-1} (ref 26).

Remarkably, the PMF along the new RC exhibits a nucleation barrier at $\xi \approx 0.8$ (Figure 4B). The barrier rationalizes why, in previous work,[26] pores in free simulations of the same system did not spontaneously close, even within a total of 10 μs of free simulation. The appearance of the nucleation barrier is in contrast to results obtained with previous RCs, which did not reveal a nucleation barrier for pore formation in membranes of DMPC[12,26,55] or of other lipids such as DLPC, DPPC, or DOPG.[12,13,16,18,26,55] Hence, the absence of the nucleation barrier in previously computed PMFs for DMPC suggests that the barrier was integrated out,[26] or in other words, the nucleation barrier was previously a "hidden barrier".[31,32]

Figure 5A presents typical simulation frames along the RC, including the flat membrane, a partial defect, and the fully formed continuous pore. Figure 5B presents three typical frames at the transition state around $\xi \approx 0.8$. In line with previous propositions,[13,26] these frames reveal that the transition state may be characterized by structures that are about to form a continuous hydrogen bond network over the membrane.

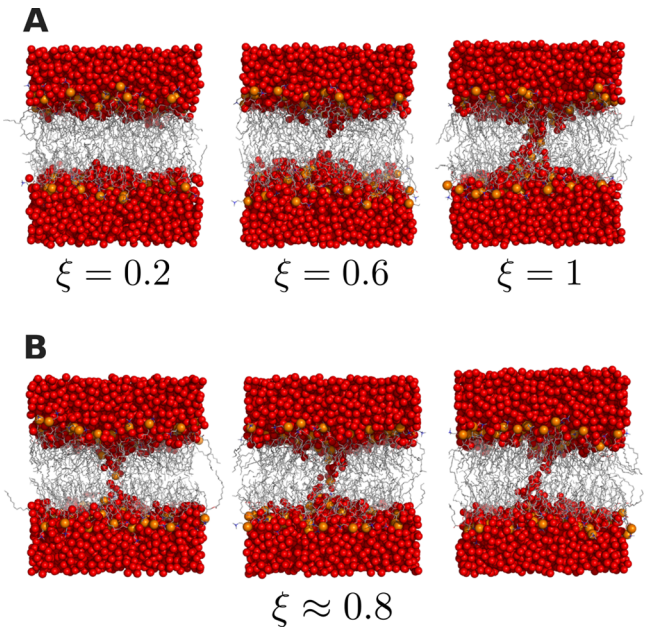

Figure 5. Typical simulation snapshots taken from the umbrella sampling simulations. Lipids are visualized as sticks, water oxygen as red spheres, and lipid phosphorus atoms as orange spheres. (A) Flat membrane (ξ = 0.2), partial defect (ξ = 0.6), and the fully formed aqueous pore (ξ = 1). (B) Typical snapshots near the transition state of pore formation ($\xi \approx 0.8$). For clarity, the atoms in all snapshots were shifted laterally such that the center of the cylinder (X_{cyl}, Y_{cyl}) is at the box center.

Convergence and Absence of Hysteresis. Since PMFs are by definition ensemble properties, the computed PMF should obviously not depend on the direction of the reaction. In practice, however, PMFs computed from MD simulations may be strongly affected by hysteresis[26] (see Introduction and Figure 1). To exclude similar hysteresis effects with the new RC, we computed PMFs along pore-opening and pore-closing pathways, similar to our previous work.[26] Accordingly, initial coordinates for umbrella sampling were either taken from a 50-ns slow-growth pore-opening simulation or from a slow-growth pore-closing simulation (see Methods). Subsequently, the PMFs were computed from different time intervals of the umbrella sampling simulations to obtain the equilibration time required to remove any influence from the pathway (opening or closing). Figure 6 demonstrates that the PMFs computed with our new RC exhibit virtually no hysteresis. Only 5 ns of equilibration were sufficient for obtaining similar PMF for pore-opening (Figure 6A) and pore-closing pathways (Figure 6B).

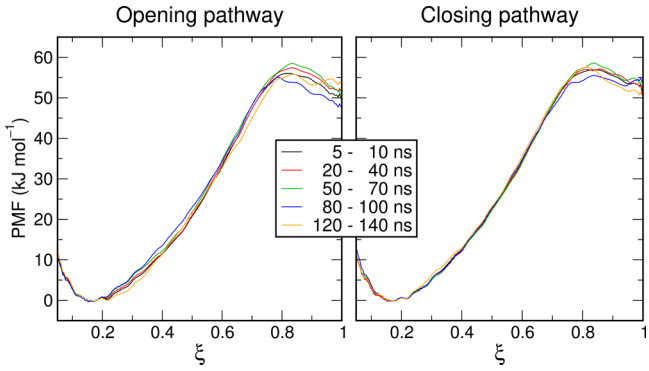

Figure 6. PMFs computed along (A) the pore-opening pathway and (B) the pore-closing pathway, using different time intervals of umbrella sampling simulations (see legend). Pore-opening and pore-closing PMFs are nearly identical, demonstrating that the calculations do not suffer from hysteresis. The PMFs were computed using the parameters ζ = 0.75, R_{cyl} = 0.8 nm, and d_s = 0.1 nm.

The absence of hysteresis suggests that the new RC was capable of restraining the system close to the transition state of pore formation. To show this more explicitly, we picked 74 simulation frames from a 140 ns umbrella window near the transition state, we triggered free simulations from these frames, and we observed whether the systems fell into the open or into the closed state during the free simulations. More specifically, frames were taken from the umbrella window restrained at ξ = 0.85, picking frames that fulfilled 0.854 < ξ < 0.856. The 74 trajectories of those free simulations are shown in Figure 7A.

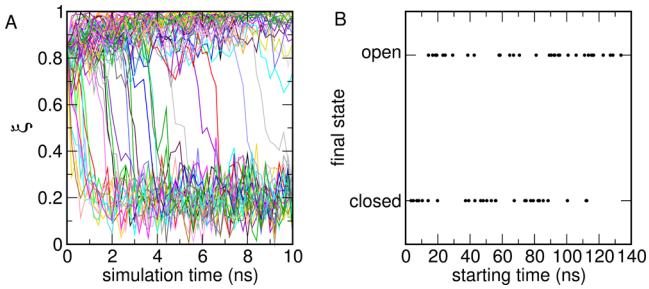

Figure 7. (A) Seventy-four trajectories of free simulations starting near the transition state. Initial frames were picked from a 140 ns umbrella window restrained at ξ = 0.85. Approximately half of the 74 simulations fell into the open state, the other half into the closed state. (B) Final state of the 74 free simulations in (A) versus the simulation time at which the initial frames was picked from the 140 ns umbrella simulation, exhibiting a short autocorrelation time. This analysis suggests that the system was restrained tightly to the transition state of pore formation. The PMFs were computed using the parameters ζ = 0.75, R_{cyl} = 0.8 nm, and d_s= 0.1 nm.

DOI: 10.1021/acs.jctc.7b00106
J. Chem. Theory Comput. 2017, 13, 2352−2366

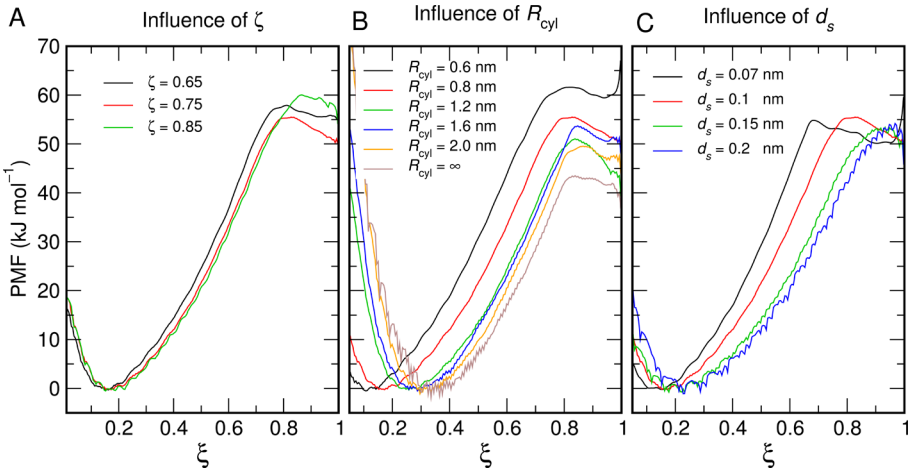

Figure 8. Influence of the parameters ζ, R_{cyl}, and d_s on the PMF of pore formation. (A) Effect of ζ (using R_{cyl} = 0.8 nm, d_s = 0.1 nm), (B) effect of R_{cyl} (using ζ = 0.75, d_s = 0.1 nm), and (C) effect of d_s (using ζ = 0.75, R_{cyl} = 0.8 nm).

Within 10 ns, approximately half of the simulations reached the state of the open pore (Figure 7A, $\xi \approx 1$), whereas the other half of the simulations fell into the state of the flat membrane (Figure 7A, $\xi \approx 0.2$). Very few simulations remained near the transitions state after 10 ns. In addition, Figure 7B summarizes the final state of these 74 free simulations versus the simulation time at which the initial frame was picked from the umbrella sampling window. The key finding is that the final state reached by the free simulations (open or closed) is hardly correlated over the simulation time at which the initial frames were picked from the umbrella window. This findings demonstrates that the umbrella simulations indeed restrain the system tightly to the transition state, rationalizing the absence of hysteresis between pore-opening and pore-closing simulations.

To assess the convergence of the PMFs with simulation time, we computed all PMFs in this study from various time intervals of the umbrella sampling simulations. We typically observed that the shape of the PMFs near the transition state ($0.7 < \xi < 1$) converged more slowly as compared to the other regions of the PMF. As an example, PMFs in Figure 6A and B were computed from 20 ns intervals, revealing some variance of the position of the main barrier. For obtaining fully converged PMFs at 323 K, we suggest to carry out umbrella sampling for 50 or 100 ns per umbrella window for such one-component lipid membranes as considered here. At 300 K, we suggest simulations of 100−150 ns per umbrella window.

Influence of the Parameters ζ, R_{cyl}, and d_s. The RC suggested here requires the definition of three parameters: ζ, R_{cyl}, and d_s (see Theory). Strictly speaking, using a different set of these parameters leads to a different RC and to a different numerical prediction for the free energy of pore formation. Using unsuitable parameters could potentially yield a poor RC with problems as described in the Introduction: (i) they could lead to an overestimate of the pore formation free energy (PMF at $\xi \approx 1$) since they would perturb the membrane more strongly that strictly required for pore formation and (ii) they could lead to a PMF that misses the barrier. In turn, PMFs computed with a good set of such parameters would yield a relatively low estimate for the free energy of the open pore, and it would reveal the pore nucleation barrier.

To identify a suitable set of parameters, we carefully tested the influence of ζ, R_{cyl}, and d_s on the PMFs (Figure 8). Here, PMFs were computed using 50 ns of simulation per umbrella window, while omitting the first 10 ns for equilibration. We found that changing ζ has a relatively small effect on the overall shape of the PMF or on the free energy of pore formation, but ζ has some effect on the PMF near the transition state (Figure 8A). On the basis of these PMFs, we used ζ = 0.75.

Changing the radius of the cylinder R_{cyl}, in contrast, may strongly influence the PMFs (Figure 8B). First, the position of the equilibrium state (PMF minimum) is shifted to larger ξ with increasing R_{cyl} (Figure 8B, $\xi \approx 0.1$ to 0.3). This finding merely reflects that, given larger R_{cyl}, equilibrium fluctuations of polar atoms near the head groups of the intact membrane have a higher chance to occupy additional slices. More critically, choosing a small R_{cyl} leads to an increased free energy of pore formation (Figure 8B, black and red curves). This finding is rationalized by the fact that a narrow cylinder confines the polar defect more strongly than required for pore formation. In turn, a very large R_{cyl} may not differentiate between (i) two laterally displaced hanging droplet structures (Figure 2B) and (ii) an continuous polar defect (Figure 2C). Consequently, the nucleation barrier is integrated out (Figure 8B, brown curve). Since the PMF computed with R_{cyl} = 1.2 nm yield a relatively small free energy of the open pore, while clearly exhibiting the nucleation barrier (Figure 8B, green curve), we suggest R_{cyl} = 1.2 nm as a reasonable value for future studies.

Figure 8C presents PMFs computed with different values for the slice thickness d_s. Using $d_s \geq 0.15$, the PMFs are still increasing near $\xi \approx 1$, suggesting that the number of polar atoms inside the defects is insufficient to form a stable hydrogen bond network over the membrane (Figure 8C, green and blue curves). In contrast, using d_s = 0.1 or 0.07 nm, the PMFs clearly resolve the nucleation barrier (Figure 8C, black and red curves). On the basis of these PMFs, we consider values d_s in the range of 0.07 to 0.1 nm as reasonable.

Comparison with Previous Reaction Coordinates. As pointed out above, PMF calculations using previously established RCs did not resolve the nucleation barrier for pore formation over a DMPC membrane,[12,55] and the calculations suffered from hysteresis between pore-opening and pore-closing simulations.[14,26,31] We proposed that the lack of a nucleation barrier indicates that restraining the system along those RCs did not restrain the systems close to the transition state of pore formation. Here, by reanalysing

DOI: 10.1021/acs.jctc.7b00106
J. Chem. Theory Comput. 2017, 13, 2352−2366

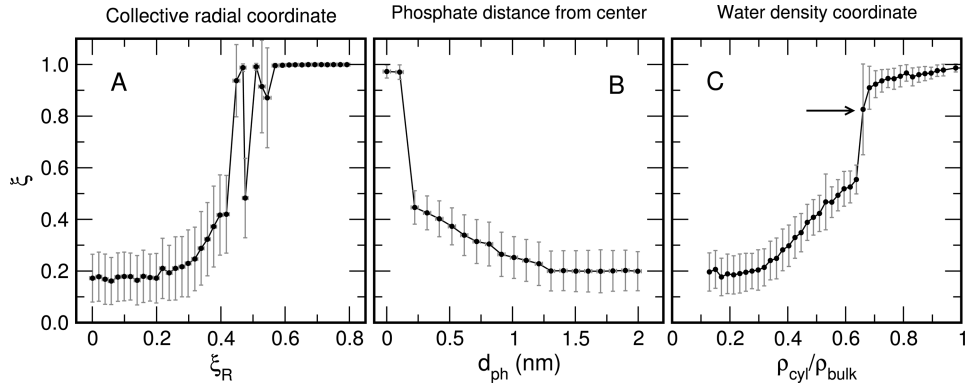

Figure 9. Comparison with umbrella sampling simulations restrained along three other reaction coordinates: (A) the collective radial coordinate ξ_R suggested by Tolpekina et al.,[15,16] (B) the distance of a single phosphate d_{ph} from the membrane center, corresponding to a lipid flip-flop,[11−13,55] and (C) the water density within a fixed membrane-spanning cylinder ρ_{cyl} relative to bulk water density, ρ_{bulk}, suggested by Mirjalili and Feig.[18] The coordinate ξ was computed using the parameters ζ = 0.75, R_{cyl} = 0.8 nm, and d_s= 0.1 nm.

umbrella sampling simulations conducted for our previous work,[26] we show explicitly that this proposition indeed holds.

Figure 9A−C presents results from umbrella sampling simulations restrained along the following three RCs: (A) the collective radial RC ξ_R suggested by Tolpekina et al.,[15] (B) the distance d_{ph} of a lipid phosphorus atom from the membrane center,[11] and (C) the average density of water ρ_{cyl} (or the number of water molecules) within a fixed membrane-spanning cylinder.[18] The symbols in Figure 9A−C show the average and standard deviation of the position along the new RC ξ computed from the umbrella sampling simulation restrained along the previous RCs ξ_R, d_{ph}, or ρ_{cyl}, respectively, where ρ_{cyl} was plotted relative to the bulk water density ρ_{bulk}. Evidently, restraining the system along the previous RCs did not lead to a complete sampling of the new RC. Instead, the systems sampled either states with a partial defect ($\xi \lesssim 0.6$) or states with a continuous transmembrane pore ($\xi \gtrsim 0.9$), but the systems did not properly sample the transition state near $\xi \approx 0.83$. Further, nearly no transitions between the partial and continuous defects were sampled.

A notable exception is the umbrella window restrained at ρ_{cyl}/ρ_{bulk} = 0.66, indicated by the arrow in Figure 9C, which deserves additional explanation. The mean position and standard deviation along ξ suggest that this window sampled the transition state. Indeed, as shown in Figure 10A, this umbrella simulation crossed the transition state twice within 500 ns, once toward the continuous defect (Figure 10A, 115 ns), and back to the partial defect (Figure 10A, 430 ns). However, all the intermediate positions close to the transition state were hardly sampled. Hence, restraining the system at ρ_{cyl}/ρ_{bulk} = 0.66 leads to a simulation that sampled two highly distinct states, namely (i) a partial defect ($\xi \approx 0.55$, Figure 10B) and (ii) a continuous polar defect ($\xi \approx 0.9$, Figure 10C), but the simulation visited the transition state only twice per 500 ns. Notably, the time scale of the transition in this window coincides with the time scale of a few hundred nanoseconds required to remove hysteresis between pore-opening and pore-closing simulations conduced with the ρ_{cyl} coordinate.[26] This finding suggests that slow transitions over the transition state are related to slow recovery from hysteresis. In turn, restraining the system close to the transition state, as possible with the new RC, enables rapid sampling of the transition state and avoids hysteresis.

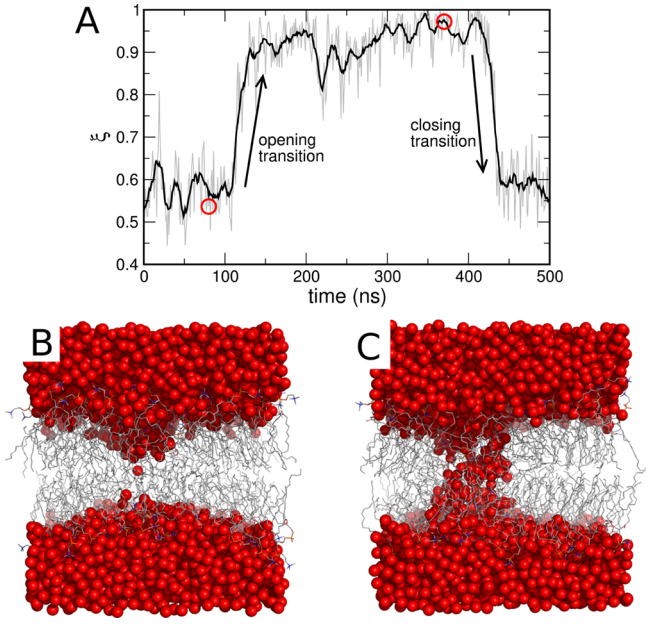

Figure 10. Analysis of a single umbrella simulation window restrained along the coordinate ρ_{water}/ρ_{bulk} = 0.66, suggested by Mirjalili and Feig.[18] (A) time trace of the umbrella simulation projected onto the new reaction coordinate. This umbrella window visited the state of a partial defect ($\xi \approx 0.55$) and of a continuous defect ($\xi \approx 0.9$), but visited the transition state only twice per 500 ns. (B) Typical snapshot of a partial defect and (C) of a continuous defect, taken from the time points highlighted by red circles in panel A.

Lipid Force Field: Influence on Metastability but Hardly on Pore Formation Free Energy. So far, we presented PMFs of pore formation purely based on the Berger lipid force field.[37] However, the metastability of the open pore as well as the free energy for pore formation may in principle depend on the force field. Previous simulations using the lipid flip-flop RC in membranes of DMPC, DPPC, and POPC observed large differences between PMFs computed with different force fields.[14,56] However, the authors attributed the differences to hysteresis, suggesting that sampling problems were partly hiding the actual force field differences.[14]

Here, we computed the PMF for pore formation over a DMPC membrane using three popular lipid force fields, namely, using the Berger force field,[37] Slipids,[49] and

DOI: 10.1021/acs.jctc.7b00106
J. Chem. Theory Comput. 2017, 13, 2352−2366

CHARMM36,[51] at temperatures of 323 K (Figure 11A) and 300 K (Figure 11B). As shown in Figure 11A and B, the PMF

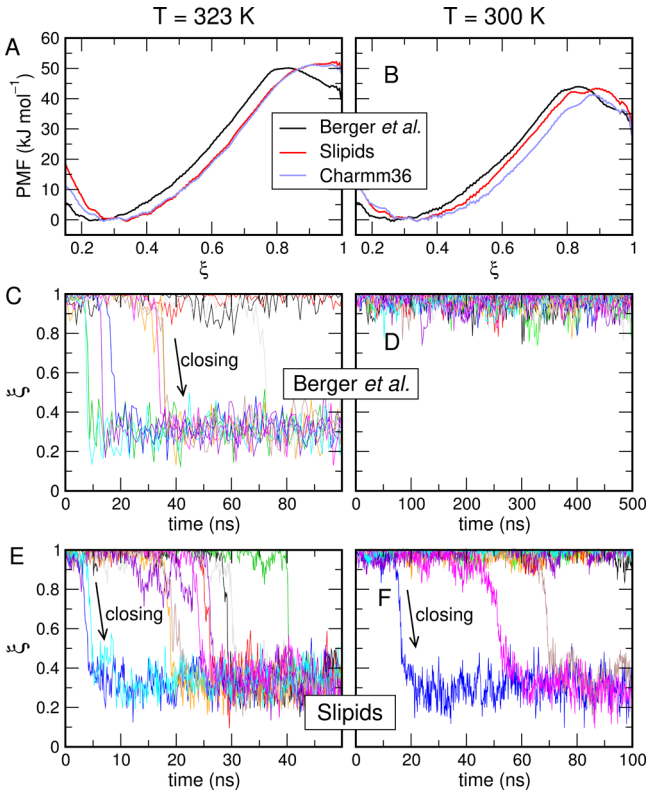

Figure 11. (A, B) PMFs of pore formation over DMPC membranes using three different lipid force fields: Berger force field[37] (black), Slipids[49] (red), and CHARMM36[51] (blue), at temperatures of (A) 323 or (B) 300 K. The Berger force fields suggests a metastable prepore state at 323 and at 300 K, whereas Slipids and CHARMM36 force fields suggest a metastable prepore state purely at 300 K. (C−F) Free simulations starting from the open pore ($\xi \approx 1$) using the Berger force field (C, D) or using Slipids (E, F), at temperatures of 323 (C, E) and 300 K (D, F). Different rates of pore closure are observed, in line with different pore nucleation barriers in the PMFs in (A, B). Note the different scaling on the time axes in (C−F). The trajectories presented in (D) were taken from previous work.[26] The coordinate ξ was computed using the parameters ζ = 0.75, R_{cyl} = 1.2 nm, and d_s= 0.1 nm.

maximum is nearly invariant with respect to the applied force field. This finding is in contrast to PMFs computed with the lipid flip-flop coordinate, which implied strongly increased free energies with the Slipids and CHARMM36 force fields for moving a headgroup to the membrane center.[56] Hence, as suggested previously,[14] the force field may influence the rate of the formation of continuous defect in simulations with a headgroup restrained close to the membrane center, leading to different PMF estimates as computed from limited simulation times. In other words, in simulations using the lipid flip-flop coordinate, the magnitude of hysteresis depends on the force field. However, as shown here, in the absence of hysteresis, PMFs are much less dependent on the force field than previously anticipated.

The presence and magnitude of the nucleation barrier depends both on the force field and the temperature (Figure 11A and B). Simulations with the Berger force field suggest metastability of the open pore both at 323 and 300 K, as indicated by the pore nucleation barrier at $\xi \approx 0.8$ and the free-energy minimum at $\xi \approx 1$ (Figure 11A and B, black). The barrier is more pronounced at 300 K as compared to 323 K. In contrast, simulations with the Slipids or CHARMM36 force fields suggest metastability at 300 K but not at 323 K (Figure 11A and B, red and blue). Taken together, the PMFs suggest that metastability but not the free energy of pore formation is force field-dependent for DMPC lipids. In addition, for all force fields, we find that lower temperatures favor metastability of the open pore, that is, lower temperatures lead to slower rates of pore closure.

To further confirm the nucleation barriers in Figure 11A and B, we carried out free simulations starting from various time frames of umbrella windows of the open pore. Ten free simulations each were conducted using either the Berger lipids (Figure 11C and D) or the Slipids (Figure 11E and F) and simulating either at a temperature of 323 K (Figure 11C and E) or at 300 K (Figure 11D and F). The trajectories of pore closure are visulalized in Figure 11D−F, and the maximum-likelihood estimates for the pore lifetime τ_{ml}, as computed from these trajectories, are summarized in Table 2. Overall, we find

Table 2. Maximum-Likelihood Estimate of Pore Lifetimes τ_{ml} from Free Simulations

lipid force field	T (K)	τ_{ml} (ns)
Berger et al.	323	53
Berger et al.	300	$\gtrsim$5000
Slipids	323	22
Slipids	300	280

that the pore lifetimes τ_{ml} are qualitatively in line with the nucleation barrier height (as measured from the state of the open pore). At 300 K, pores in Slipid simulations close with a relatively long lifetime of 280 ns and pores in Berger simulations do not close even within a total simulation time of 5000 ns, in line with the more pronounced barriers in the PMF at 300 K (Figure 11B, black and red). At 323 K, pores in Slipids simulations close rapidly with a lifetime of only 22 ns, in line with the absence of a pore nucleation barrier (Figure 11B, red), and the pores in Berger simulations close within 53 ns, in line with the reduced barrier as compared to the 300 K simulations. However, we also note that the closure rates do not quantitatively agree with the rates suggested by the barrier height using a simple transition state ansatz. This may indicate that the PMFs in Figure 11A and B are not yet fully converged, or that the barrier is still partly integrated out, even with the new reaction coordinate. Nevertheless, the qualitative correspondence between barrier weighs and closure rates provide additional evidence that the PMFs in Figure 11A indeed reflect the free energy landscape of pore formation.

Membrane Size: Influence on Metastability, but Hardly on Pore Formation Free Energy. When simulating a very small membrane, the entire membrane between a pore and its periodic image may be highly bent, which influences the free energy landscape of pore formation. Indeed, in previous simulations with the Berger force field, we found that the pore in a membrane of 64 DMPC lipids spontaneously closed, whereas the pore in a membrane of 128 lipids remained open for at least 10 μs.[26] To rationalize these previous findings in energetic terms, we computed the PMFs with the new RC using membranes of 64, 96, 128, and 162 lipids (Figure 12) modeled with the Berger force field. Evidently, the membrane

DOI: 10.1021/acs.jctc.7b00106
J. Chem. Theory Comput. 2017, 13, 2352−2366

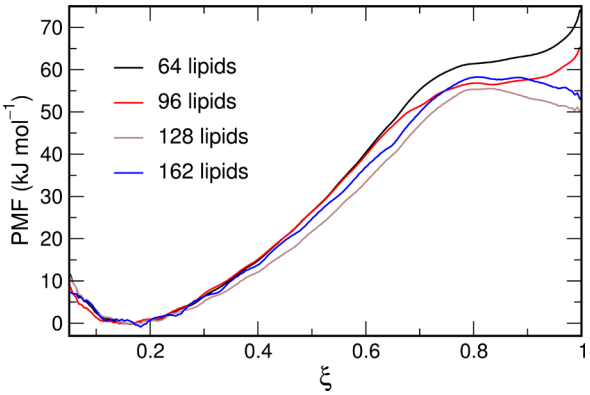

Figure 12. PMFs for pore formation in DMPC using the Berger force field and using systems of 64, 96, 128, or 162 lipids (see legend). In small systems, the open pore is not metastable, probably because of a highly bent membrane between the pore and its periodic image, and the pore formation free energy is slightly increased. The coordinate ξ was computed using the parameters ζ = 0.75, R_{cyl} = 0.8 nm, and d_s= 0.1 nm.

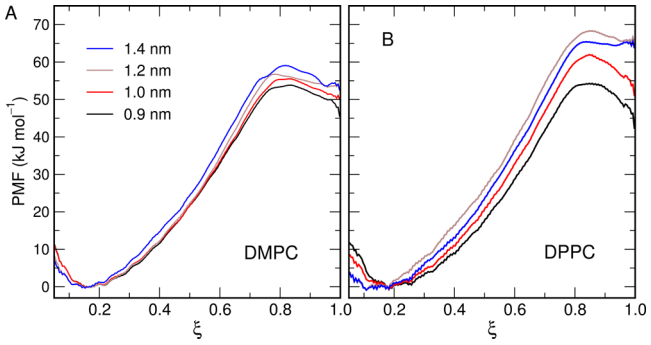

Figure 13. PMFs for pore formation in (A) DMPC and (B) DPPC using the Berger force field and using Lennard-Jones cutoff distances between 0.9 and 1.4 nm (see legend). In DMPC, the cutoff has only a small influence on the PMFs in the absence of hysteresis. In DPPC, however, the cutoff has a larger effect on the PMFs. The coordinate ξ was computed using the parameters ζ = 0.75, R_{cyl} = 0.8 nm, and d_s= 0.1 nm. N_s = 26 slices were used for DMPC, and N_s = 30 for DPPC.

size has a relatively small influence on the free energies of pore formation in DMPC. However, using small systems of 64 or 96 lipids, the open pore is not metastable, as indicated by the absence of a PMF minimum at ξ = 1 (Figure 12, black and red), and in contrast to membranes of 128 or 162 lipids (Figure 12, brown and blue). These PMFs provide the energetic rationale for the spontaneous pore closure in simulations of 64 DMPC lipids in previous work.[26] On the basis of these PMFs, we suggest to use membrane systems of at least 128 lipids for simulations of narrow pores over DMPC membranes considered here. However, for lipids with longer tails as compared to DMPC membranes or for membranes containing cholesterol, we cannot exclude that larger membrane systems are required to avoid finite-size artifacts.

Small Effects from Truncation of Van-der-Waals Interactions. It is well established that the cutoff distance used for truncating Lennard-Jones (LJ) interactions may influence various membrane properties, such as the area per lipid, surface tension, or order parameters.[14,57] Huang and Garcia reported large influence of the LJ cutoff on PMFs along the lipid flip-flop coordinate d_{ph} in a DPPC membrane modeled with the Berger force field.[14] The LJ cutoffs influenced the PMF mainly because a shorter cutoff facilitated the formation of a continuous water defect over the membrane, leading to a flat PMF if the phosphorus atom was near the membrane center ($d_{ph} \approx 0$). In contrast, no such continuous water defect formed within simulation time when using longer cutoffs, leading to an ever increasing PMF as the phosphorus atom was pulled to the membrane center and even into the opposite leaflet. Hence, as discussed by the authors,[14] hysteresis (i.e., sampling problems) are more dominant with longer cutoffs when using the d_{ph} RC. However, it remained unclear to which extent the true underlying PMF (assuming no sampling problems) is influenced by the LJ cutoffs.

Therefore, using the new RC, we revisited the influence of the LJ cutoff on the PMF of pore formation. Figures 13A and 13B present PMFs for pore formation over membranes of 128 DMPC lipids or 128 DPPC lipids, respectively, respectively, each modeled with the Berger force field and using LJ cutoffs of 0.9, 1.0, 1.2, or 1.4 nm. The DPPC system was set up as described for DMPC systems in the Methods. We found that the free energy of pore formation depends more strongly on the cutoff in DPPC as compared to DMPC. For DMPC, we found that using longer LJ cutoffs of 1.2 or 1.4 nm, the free energy of pore formation is increased by only ~4 kJ mol^{-1}, as compared to simulations with a 0.9 or 1.0 nm cutoff. For DPPC, in contrast, the free energy of pore formation may vary by up to 14 kJ mol^{-1} upon varying the cutoff between 0.9 and 1.4 nm. However, these cutoff effects in DPPC are smaller as compared to the effects based on the flip-flop coordinate,[14] suggesting that cutoff effect on previous PMFs for DPPC were partly a consequence of hysteresis, in line with the interpretation by Huang and Garcia.[14] Since the PMF for DPPC with the 0.9 nm cutoff appears to represent an outlier, we do not recommend the short 0.9 nm cutoff for future studies. In contrast, the differences between the PMFs with a cutoff ≥1.0 nm are probably within the accuracy of the force field, suggesting that a cutoff of 1.0 nm provides a reasonable balance between accuracy and simulation speed for the simulations with the Berger force field considered here. Overall, if we avoid the shortest 0.9 nm cutoff, the LJ cutoff seems to have a relatively small effect on the PMF of pore formation.

CONCLUSIONS

We have developed and implemented a new reaction coordinate (RC) that is capable of probing the formation or rupture of a continuous polar defect over a lipid membrane. We showed that the new RC may be used for PMF calculations of pore formation using the technique of umbrella sampling. The PMFs converged rapidly and exhibited virtually no hysteresis between pore-opening and pore-closing simulations, in contrast to PMF calculations with previously established RCs. The absence of hysteresis is a consequence of the key property of the RC, namely that it is capable of restraining the system close to the transition state of pore formation.

The favorable properties of the RC are, we believe, a consequence of three design elements: (a) The RC does *not* probe the total number of polar atoms inside the membrane or inside a membrane-spanning cylinder,[18] but instead the number of slices along the membrane normal that are occupied by at least one polar atom. Consequently, the RC may differentiate between structures of (i) a large asymmetric defect spanning only one leaflet (the "hanging droplet" structure, Figure 2A) and (ii) a thin continuous aqueous pore spanning the complete

DOI: 10.1021/acs.jctc.7b00106
J. Chem. Theory Comput. 2017, 13, 2352−2366

bilayer (Figure 2C). Such asymmetric hanging droplet structures may be stabilized by membrane undulation and, hence, are a major source of hysteresis in simulations of pore formation.[14,31] (b) Only the atoms within a membrane-spanning cylinder contribute to the RC proposed here, a feature already suggested by Mirjalili and Feig.[18] This property is crucial to avoid the formation of two laterally displaced partial defects in opposite leaflets (Figure 2B). Such laterally displaced defects are likewise stabilized by membrane undulation, and they are another source of hysteresis. (c) The position of the membrane-spanning cylinder in the membrane plane is not fixed at an arbitrary position. Instead, the center of the cylinder (X_{cyl}/Y_{cyl}) is dynamically defined, thereby allowing the cylinder to move as the defect drifts in the membrane plane. Consequently, the system cannot move along the RC by shifting the defect laterally out of the cylinder, which we identified as a source for hysteresis when using the RC by Mirjalili and Feig (see Figure 10).[18,26] Notably, we defined (X_{cyl}/Y_{cyl}) using a center of mass definition that remains well-defined in systems of periodic boundary conditions (eqs 10−12). This definition avoids an ill-defined center of mass if the defect travels over the periodic boundary. Taken together, the RC proposed here avoids by design several common sources of undesired hysteresis in simulations of pore formation.

Decades ago, Abidor et al. hypothesized that the nucleation of a transmembrane pore involves a free energy barrier.[20] Accordingly, the open pore would form a metastable prepore state. The existence of such prepore states in tension-free membranes has remained controversial because PMF calculations using previous RCs did not resolve any free energy barrier between the states of the intact membrane and the open pore.[12,15,16,26,55] Here, using the new RC, we showed that such prepore states over a DMPC membrane may indeed be metastable, and we determined the barrier height to a few kilojoule per mole when using the Berger force field. We noted that the magnitude of the nucleation barrier depends not only on temperature, but also on the applied lipid force field, suggesting that the magnitude of the barrier under experimental conditions remains to be clarified. However, PMF calculations with the new RC provide a route for a systematic analysis of the physicochemical determinants of the long-discussed prepore state.

Using the new RC, we have systematically analyzed the influence of (i) the lipid force field, (ii) the cutoff distance used for Lennard-Jones (LJ) interactions, and (iii) system size on the PMF of pore formation over a DMPC membrane. Previous work suggested a large influence from such parameters.[14,34,56] With the new RC, in contrast, we found that the force field, LJ cutoff distance, and membrane size have a relatively small effect on the free energies of pore nucleation. Hence, it is reasonable to believe that larger effects reported previously[14,34,56] were a consequence of using other RCs, possibly leading to different degrees of hysteresis with different choices for such parameters. However, we found that the metastability of the open pore in DMPC may depend on such parameters. Specifically, the pore was metastable when simulating a larger membrane with the Berger lipids, but the pore was unstable with the Slipids or CHARMM36 force fields at 323 K, or when simulating a small membrane.

This Article focused on establishing and testing the new RC. Yet the RC is well suitable to probe the impact of various external factors, with impact on a range of biophysical questions. For instance, it will be highly interesting to test the influence of lipid composition, membrane-active peptides, or peptide fragments, membrane hydration, tension, or electric fields on pore formation. The RC may be used for studying pore formation during membrane fusion. In addition, membrane permeation of highly polar solutes, in particular of ions, typically involve the formation of aqueous defects. We therefore believe that simulations of solute permeation will benefit from the RC presented here. Such future efforts may provide a route for a quantitative understanding of the role of pore formation in membrane biophysics.

APPENDIX

Atomic Forces Derived from Pulling along the Reaction Coordinate

Derivatives of the Reaction Coordinate (RC). The simulation system can be pulled or restrained along the RC ξ by applying the harmonic biasing potential $V = k(\xi - \xi_0)^2/2$, leading to a force along ξ of $F_\xi = -\partial V/\partial\xi = -k(\xi-\xi_0)$, where ξ_0 is the reference position along ξ. The force F_ξ translates to forces acting on the atoms via the chain rule, $\mathbf{F}_j = F_\xi \cdot \partial\,\xi/\partial\,\mathbf{r}_j$, where j is the atomic index. Using eqs 1−4, we have

$$\frac{\partial\xi}{\partial\mathbf{r}_j} = N_s^{-1}\sum_{s=0}^{N_s-1}\psi'(N_s^{(p)};\,\zeta)\sum_{i=1}^{N^{(p)}} \frac{\partial f}{\partial\mathbf{r}_j}(\mathbf{r}_i,\,z_s,\,d_s,\,X_{cyl},\,Y_{cyl},\,R_{cyl}) \tag{13}$$

where ψ' denotes the derivative of the switch function ψ (eq 3). Evaluating the derivatives requires some care since the center of the cylinder (X_{cyl}, Y_{cyl}) depends on the atomic coordinates. Using eq 5, we get

$$\frac{\partial f(\mathbf{r}_i,\,z_s,\,\ldots)}{\partial\mathbf{r}_j} = f_{axial}(z_i,\,z_s,\,d_s)\frac{\partial}{\partial\mathbf{r}_j}f_{radial}(\mathbf{r}_i) + f_{radial}(\mathbf{r}_i)\frac{\partial}{\partial\mathbf{r}_j}f_{axial}(z_i,\,z_s,\,d_s) \tag{14}$$

To evaluate the gradients in eq 14, note that f_{axial} depends on z_j but not on x_j or y_j, whereas f_{radial} depends on x_j, y_j and z_j, since the (X_{cyl}, Y_{cyl}) depend on z_j. We obtain

$$\frac{\partial}{\partial\mathbf{r}_j}f_{radial}(\mathbf{r}_i) = \theta'\left(\frac{r_i}{R_{cyl}},\,h\right)\frac{1}{R_{cyl}r_i}\begin{pmatrix}(x_i - X_{cyl})\left(\delta_{ij} - \dfrac{\partial X_{cyl}}{\partial x_j}\right)\\ (y_i - Y_{cyl})\left(\delta_{ij} - \dfrac{\partial Y_{cyl}}{\partial y_j}\right)\\ -(x_i - X_{cyl})\dfrac{\partial X_{cyl}}{\partial z_j} - (y_i - Y_{cyl})\dfrac{\partial Y_{cyl}}{\partial z_j}\end{pmatrix} \tag{15}$$

DOI: 10.1021/acs.jctc.7b00106
J. Chem. Theory Comput. 2017, 13, 2352−2366

$$\frac{\partial}{\partial \mathbf{r}_j} f_{\text{axial}}(z_i, z_s, d_s) = \begin{pmatrix} 0 \\ 0 \\ \delta_{ij}\theta'\left(\frac{z_i - z_s}{d_s/2}, h\right)\frac{2}{d_s} \end{pmatrix} \tag{16}$$

where we used for eq 15 that $\partial X_{\text{cyl}}/\partial y_j = \partial Y_{\text{cyl}}/\partial x_j = 0$. The symbol δ_{ij} denotes the Kronecker delta. The symbol θ' denotes the derivative of the continuous switch function θ (eq 6), given by

$$\theta'(x, h) = \begin{cases} -\frac{3}{4h} + \frac{3}{4h^3}(x-1)^2 & \text{if } 1 - h < x < 1 + h \\ +\frac{3}{4h} - \frac{3}{4h^3}(x+1)^2 & \text{if } -1 - h < x < -1 + h \\ 0 & \text{otherwise} \end{cases} \tag{17}$$

Taking the sum over i in eq 13 and using eq 14, we obtain

$$\sum_{i=1}^{N^{(p)}} f_{\text{axial}}(z_i, z_s, d_s)\frac{\partial f_{\text{radial}}(\mathbf{r}_i)}{\partial \mathbf{r}_j} = f_{\text{axial}}(z_j, z_s, d_s)\theta'\left(\frac{r_j}{R_{\text{cyl}}}, h\right)\frac{1}{R_{\text{cyl}} r_j}\begin{pmatrix} x_j - X_{\text{cyl}} \\ y_j - Y_{\text{cyl}} \\ 0 \end{pmatrix} - \begin{pmatrix} \frac{\partial X_{\text{cyl}}}{\partial x_j}A_s^x \\ \frac{\partial Y_{\text{cyl}}}{\partial y_j}A_s^y \\ \frac{\partial X_{\text{cyl}}}{\partial z_j}A_s^x + \frac{\partial Y_{\text{cyl}}}{\partial z_j}A_s^y \end{pmatrix} \tag{18}$$

and

$$\sum_{i=1}^{N^{(p)}} f_{\text{radial}}(\mathbf{r}_i)\frac{\partial f_{\text{axial}}(z_i, z_s, d_s)}{\partial z_j} = f_{\text{radial}}(\mathbf{r}_j)\theta'\left(\frac{z_j - z_s}{d_s/2}, h\right)\frac{2}{d_s} \tag{19}$$

where we introduced the abbreviation

$$\begin{pmatrix} A_s^x \\ A_s^y \end{pmatrix} := \sum_{i=1}^{N^{(p)}} f_{\text{axial}}(z_i, z_s, d_s)\theta'\left(\frac{r_i}{R_{\text{cyl}}}, h\right)\frac{1}{R_{\text{cyl}} r_i}\begin{pmatrix} x_i - X_{\text{cyl}} \\ y_i - Y_{\text{cyl}} \end{pmatrix} \tag{20}$$

Derivatives of the Cylinder Center. Evaluating eq 18 requires the derivatives of the lateral position of the cylinder axis X_{cyl} and Y_{cyl} with respect to the atomic coordinates. Let us first define the average over the sine and cosine functions for each slice s, weighted by the indicator function f_{axial}

$$\begin{pmatrix} \overline{s}_x^{(s)} \\ \overline{c}_x^{(s)} \end{pmatrix} := F_s^{-1}\sum_{i=1}^{N^{(p)}} f_{\text{axial}}(z_i, z_s, d_s)\begin{pmatrix} \sin(2\pi x_i/L_x) \\ \cos(2\pi x_i/L_x) \end{pmatrix} \tag{21}$$

$$\begin{pmatrix} \overline{s}_y^{(s)} \\ \overline{c}_y^{(s)} \end{pmatrix} := F_s^{-1}\sum_{i=1}^{N^{(p)}} f_{\text{axial}}(z_i, z_s, d_s)\begin{pmatrix} \sin(2\pi y_i/L_y) \\ \cos(2\pi y_i/L_y) \end{pmatrix} \tag{22}$$

With these abbreviations, eq 10 takes the form

$$\begin{pmatrix} X_{\text{cyl}}^{\sin} \\ X_{\text{cyl}}^{\cos} \end{pmatrix} = W^{-1}\sum_{s=0}^{N_s-1} w_s^{(\text{cyl})}\begin{pmatrix} \overline{s}_x^{(s)} \\ \overline{c}_x^{(s)} \end{pmatrix} \tag{23}$$

Likewise, to compute Y_{cyl}, we define

$$\begin{pmatrix} Y_{\text{cyl}}^{\sin} \\ Y_{\text{cyl}}^{\cos} \end{pmatrix} = W^{-1}\sum_{s=0}^{N_s-1} w_s^{(\text{cyl})}\begin{pmatrix} \overline{s}_y^{(s)} \\ \overline{c}_y^{(s)} \end{pmatrix} \tag{24}$$

The derivates of $\overline{s}_x^{(s)}$ and $\overline{c}_x^{(s)}$ with respect to the Cartesian coordinates of atom j are

$$\frac{\partial}{\partial x_j}\begin{pmatrix} \overline{s}_x^{(s)} \\ \overline{c}_x^{(s)} \end{pmatrix} = \frac{1}{F_s} f_{\text{axial}}(z_j, z_s, d_s)\frac{2\pi}{L_x}\begin{pmatrix} +\cos(2\pi x_j/L_x) \\ -\sin(2\pi x_j/L_x) \end{pmatrix} \tag{25}$$

$$\frac{\partial}{\partial y_j}\begin{pmatrix} \overline{s}_x^{(s)} \\ \overline{c}_x^{(s)} \end{pmatrix} = 0 \tag{26}$$

$$\frac{\partial}{\partial z_j}\begin{pmatrix} \overline{s}_x^{(s)} \\ \overline{c}_x^{(s)} \end{pmatrix} = \frac{1}{F_s}\frac{\partial f_{\text{axial}}(z_j, z_s, d_s)}{\partial z_j}\begin{pmatrix} \sin(2\pi x_j/L_x) - \overline{s}_x^{(s)} \\ \cos(2\pi x_j/L_x) - \overline{c}_x^{(s)} \end{pmatrix} \tag{27}$$

The derivatives of $s_y^{(s)}$ and $c_y^{(s)}$ are computed analogous to eqs 25 to 27 by replacing x_j and L_x with y_j and L_y, respectively. For eqs 27, we used that the derivative of a weighted average, $\langle A\rangle = (\sum_i v_i)^{-1}(\sum_i v_i A_i)$, with respect to one of the weights v_j is given by

$$\frac{\partial}{\partial v_j}\langle A\rangle = (\sum_i v_i)^{-1}(A_j - \langle A\rangle) \tag{28}$$

For the derivatives of the weights $w_s^{(\text{cyl})}$, as defined in eq 11, and of the normalization constant $W := \sum_s w_s^{(\text{cyl})}$ we have

$$\frac{\partial w_s^{(\text{cyl})}}{\partial z_j} = (1 - \tanh^2(F_s))\frac{\partial f_{\text{axial}}(z_j, z_s, d_s)}{\partial z_j} \tag{29}$$

$$\frac{\partial W}{\partial z_j} = \sum_{s=0}^{N_s-1}\frac{\partial w_s^{(\text{cyl})}}{\partial z_j} \tag{30}$$

and $\partial w_s^{(\text{cyl})}/\partial x_j = \partial w_s^{(\text{cyl})}/\partial y_j = 0$. The derivaties of $X_{\text{cyl}}^{\sin}$ and $X_{\text{cyl}}^{\cos}$, as defined in eq 23, are

$$\frac{\partial}{\partial x_j}\begin{pmatrix} X_{\text{cyl}}^{\sin} \\ X_{\text{cyl}}^{\cos} \end{pmatrix} = \frac{1}{W}\sum_{s=0}^{N_s-1} w_s^{(\text{cyl})}\frac{\partial}{\partial x_j}\begin{pmatrix} \overline{s}_x^{(s)} \\ \overline{c}_x^{(s)} \end{pmatrix} \tag{31}$$

$$\frac{\partial}{\partial y_j}\begin{pmatrix} X_{\text{cyl}}^{\sin} \\ X_{\text{cyl}}^{\cos} \end{pmatrix} = 0 \tag{32}$$

$$\frac{\partial}{\partial z_j}\begin{pmatrix} X_{\text{cyl}}^{\sin} \\ X_{\text{cyl}}^{\cos} \end{pmatrix} = \frac{1}{W}\sum_{s=0}^{N_s-1}\left[w_s^{(\text{cyl})}\frac{\partial}{\partial z_j}\begin{pmatrix} \overline{s}_x^{(s)} \\ \overline{c}_x^{(s)} \end{pmatrix} + \frac{\partial w_s^{(\text{cyl})}}{\partial z_j}\begin{pmatrix} \overline{s}_x^{(s)} - X_{\text{cyl}}^{\sin} \\ \overline{c}_x^{(s)} - X_{\text{cyl}}^{\cos} \end{pmatrix}\right] \tag{33}$$

The derivatives of $Y_{\text{cyl}}^{\sin}$ and $Y_{\text{cyl}}^{\cos}$ are analogous to eqs 31−33. Eqs 31−33 are evaluated using eqs 21−27 and 29. To obtain the

DOI: 10.1021/acs.jctc.7b00106
J. Chem. Theory Comput. 2017, 13, 2352−2366

derivatives of the X_{cyl} and Y_{cyl}, we use the derivative of the atan2 function given by

$$\frac{\partial}{\partial a}\text{atan2}(y, x) = \frac{1}{x^2 + y^2}\left(-y\frac{\partial x}{\partial a} + x\frac{\partial y}{\partial a}\right) \tag{34}$$

Using eq 34, we finally obtain

$$\frac{\partial X_{cyl}}{\partial x_j} = \frac{L_x}{2\pi}\frac{1}{(X_{cyl}^{sin})^2 + (X_{cyl}^{cos})^2}\left(-X_{cyl}^{sin}\frac{\partial X_{cyl}^{cos}}{\partial x_j} + X_{cyl}^{cos}\frac{\partial X_{cyl}^{sin}}{\partial x_j}\right) \tag{35}$$

$$\frac{\partial Y_{cyl}}{\partial y_j} = \frac{L_y}{2\pi}\frac{1}{(Y_{cyl}^{sin})^2 + (Y_{cyl}^{cos})^2}\left(-Y_{cyl}^{sin}\frac{\partial Y_{cyl}^{cos}}{\partial y_j} + Y_{cyl}^{cos}\frac{\partial Y_{cyl}^{sin}}{\partial y_j}\right) \tag{36}$$

$$\frac{\partial X_{cyl}}{\partial z_j} = \frac{L_x}{2\pi}\frac{1}{(X_{cyl}^{sin})^2 + (X_{cyl}^{cos})^2}\left(-X_{cyl}^{sin}\frac{\partial X_{cyl}^{cos}}{\partial z_j} + X_{cyl}^{cos}\frac{\partial X_{cyl}^{sin}}{\partial z_j}\right) \tag{37}$$

$$\frac{\partial Y_{cyl}}{\partial z_j} = \frac{L_y}{2\pi}\frac{1}{(Y_{cyl}^{sin})^2 + (Y_{cyl}^{cos})^2}\left(-Y_{cyl}^{sin}\frac{\partial Y_{cyl}^{cos}}{\partial z_j} + Y_{cyl}^{cos}\frac{\partial Y_{cyl}^{sin}}{\partial z_j}\right) \tag{38}$$

as well as $\partial X_{cyl}/\partial y_j = \partial Y_{cyl}/\partial x_j = 0$. These derivatives are used in eq 18 for obtaining the derivatives of the radial indicator function $f_{radial}(\mathbf{r}_i)$. The terms $[(X_{cyl}^{sin})^2 + (X_{cyl}^{cos})^2]^{-1}$ and $[(Y_{cyl}^{sin})^2 + (Y_{cyl}^{cos})^2]^{-1}$ in eqs 35−38 may lead to very rare numerical instabilities. These terms typically fluctuate around values of 10 or 1 for systems of a flat membrane or of a fully formed defect, respectively. Hence, to avoid such rare instabilities, we truncated these terms at a value of 500, thus yielding numerically stable simulations.

AUTHOR INFORMATION

Corresponding Author

*E-mail: jhub@gwdg.de.

ORCID

Jochen S. Hub: 0000-0001-7716-1767

Notes

The authors declare no competing financial interest.

ACKNOWLEDGMENTS

We thank Kalina Atkovska for critically reading the manuscript. Financial support by the Deutsche Forschungsgemeinschaft is gratefully acknowledged (SFB 803/A12 and HU 1971-1/1). N.A. was also supported by a Dorothea Schloezer fellowship.

REFERENCES

(1) Brogden, K. A. Antimicrobial peptides: pore formers or metabolic inhibitors in bacteria? *Nat. Rev. Microbiol.* **2005**, *3*, 238−250.

(2) Jahn, R.; Lang, T.; Südhof, T. C. Membrane fusion. *Cell* **2003**, *112*, 519−533.

(3) Risselada, H. J.; Grubmüller, H. How SNARE molecules mediate membrane fusion: recent insights from molecular simulations. *Curr. Opin. Struct. Biol.* **2012**, *22*, 187−196.

(4) Kägi, D.; Ledermann, B.; Bürki, K.; Seiler, P.; Odermatt, B.; Olsen, K. J.; Podack, E. R.; Zinkernagel, R. M.; Hengartner, H. Cytotoxicity mediated by T cells and natural killer cells is greatly impaired in perforin-deficient mice. *Nature* **1994**, *369*, 31−37.

(5) Neumann, E.; Schaefer-Ridder, M.; Wang, Y.; Hofschneider, P. Gene transfer into mouse lyoma cells by electroporation in high electric fields. *EMBO J.* **1982**, *1*, 841.

(6) Böckmann, R. A.; de Groot, B. L.; Kakorin, S.; Neumann, E.; Grubmüller, H. Kinetics, statistics, and energetics of lipid membrane electroporation studied by molecular dynamics simulations. *Biophys. J.* **2008**, *95*, 1837−1850.

(7) Tieleman, D. P.; Leontiadou, H.; Mark, A. E.; Marrink, S.-J. Simulation of pore formation in lipid bilayers by mechanical stress and electric fields. *J. Am. Chem. Soc.* **2003**, *125*, 6382−6383.

(8) Leontiadou, H.; Mark, A. E.; Marrink, S. J. Molecular dynamics simulations of hydrophilic pores in lipid bilayers. *Biophys. J.* **2004**, *86*, 2156−2164.

(9) Tieleman, D. P. The molecular basis of electroporation. *BMC Biochem* **2004**, *5*, 10.

(10) Piggot, T. J.; Holdbrook, D. A.; Khalid, S. Electroporation of the E. coli and S. aureus membranes: molecular dynamics simulations of complex bacterial membranes. *J. Phys. Chem. B* **2011**, *115*, 13381−13388.

(11) Tieleman, D. P.; Marrink, S.-J. Lipids out of equilibrium: Energetics of desorption and pore mediated flip-flop. *J. Am. Chem. Soc.* **2006**, *128*, 12462−12467.

(12) Bennett, W. D.; Tieleman, D. P. Water defect and pore formation in atomistic and coarse-grained lipid membranes: pushing the limits of coarse graining. *J. Chem. Theory Comput.* **2011**, *7*, 2981−2988.

(13) Bennett, W. D.; Sapay, N.; Tieleman, D. P. Atomistic simulations of pore formation and closure in lipid bilayers. *Biophys. J.* **2014**, *106*, 210−219.

(14) Huang, K.; García, A. E. Effects of truncating van der Waals interactions in lipid bilayer simulations. *J. Chem. Phys.* **2014**, *141*, 105101.

(15) Tolpekina, T.; Den Otter, W.; Briels, W. Nucleation free energy of pore formation in an amphiphilic bilayer studied by molecular dynamics simulations. *J. Chem. Phys.* **2004**, *121*, 12060−12066.

(16) Wohlert, J.; den Otter, W.; Edholm, O.; Briels, W. Free energy of a trans-membrane pore calculated from atomistic molecular dynamics simulations. *J. Chem. Phys.* **2006**, *124*, 154905.

(17) Hu, Y.; Sinha, S. K.; Patel, S. Investigating hydrophilic pores in model lipid bilayers using molecular simulations: correlating bilayer properties with pore-formation thermodynamics. *Langmuir* **2015**, *31*, 6615−6631.

(18) Mirjalili, V.; Feig, M. Density-Biased Sampling: A Robust Computational Method for Studying Pore Formation in Membranes. *J. Chem. Theory Comput.* **2015**, *11*, 343−350.

(19) Neale, C.; Madill, C.; Rauscher, S.; Pomès, R. Accelerating convergence in molecular dynamics simulations of solutes in lipid membranes by conducting a random walk along the bilayer normal. *J. Chem. Theory Comput.* **2013**, *9*, 3686−3703.

(20) Abiror, I.; Arakelyan, V.; Chernomordik, L.; Chizmadzhev, Y. A.; Pastushenko, V.; Tarasevich, M. Electric breakdown of bilayer lipid membranes I. The main experimental facts and their qualitative discussion. *Bioelectrochem. Bioenerg.* **1979**, *6*, 37−52.

(21) Zhelev, D. V.; Needham, D. Tension-stabilized pores in giant vesicles: determination of pore size and pore line tension. *Biochim. Biophys. Acta, Biomembr.* **1993**, *1147*, 89−104.

(22) Brochard-Wyart, F.; De Gennes, P.; Sandre, O. Transient pores in stretched vesicles: role of leak-out. *Phys. A* **2000**, *278*, 32−51.

(23) Karatekin, E.; Sandre, O.; Guitouni, H.; Borghi, N.; Puech, P.-H.; Brochard-Wyart, F. Cascades of transient pores in giant vesicles: line tension and transport. *Biophys. J.* **2003**, *84*, 1734−1749.

(24) Moroz, J. D.; Nelson, P. Dynamically-stabilized pores in bilayer membranes. *Biophys. J.* **1997**, *72*, 2211−2216.

(25) Tolpekina, T.; den Otter, W.; Briels, W. Simulations of stable pores in membranes: system size dependence and line tension. *J. Chem. Phys.* **2004**, *121*, 8014−8020.

(26) Awasthi, N.; Hub, J. S. Simulations of pore formation in lipid membranes: reaction coordinates, convergence, hysteresis, and finite-size effects. *J. Chem. Theory Comput.* **2016**, *12*, 3261−3269.

DOI: 10.1021/acs.jctc.7b00106
J. Chem. Theory Comput. 2017, 13, 2352−2366

(27) Neale, C.; Hsu, J. C.; Yip, C. M.; Pomès, R. R. Indolicidin binding induces thinning of a lipid bilayer. *Biophys. J.* **2014**, *106*, L29−L31.
(28) Bolhuis, P. G.; Chandler, D.; Dellago, C.; Geissler, P. L. Transition path sampling: Throwing ropes over rough mountain passes, in the dark. *Annu. Rev. Phys. Chem.* **2002**, *53*, 291−318.
(29) Best, R. B.; Hummer, G. Reaction coordinates and rates from transition paths. *Proc. Natl. Acad. Sci. U. S. A.* **2005**, *102*, 6732−6737.
(30) Romo, T. D.; Grossfield, A. Unknown unknowns: the challenge of systematic and statistical error in molecular dynamics simulations. *Biophys. J.* **2014**, *106*, 1553−1554.
(31) Neale, C.; Bennett, W. D.; Tieleman, D. P.; Pomès, R. Statistical convergence of equilibrium properties in simulations of molecular solutes embedded in lipid bilayers. *J. Chem. Theory Comput.* **2011**, *7*, 4175−4188.
(32) Neale, C.; Pomès, R. Sampling errors in free energy simulations of small molecules in lipid bilayers. *Biochim. Biophys. Acta, Biomembr.* **2016**, *1858*, 2539−2548.
(33) Weinan, E.; Ren, W.; Vanden-Eijnden, E. String method for the study of rare events. *Phys. Rev. B: Condens. Matter Mater. Phys.* **2002**, *66*, 052301.
(34) Hu, Y.; Ou, S.; Patel, S. Free energetics of arginine permeation into model DMPC lipid bilayers: coupling of effective counterion concentration and lateral bilayer dimensions. *J. Phys. Chem. B* **2013**, *117*, 11641−11653.
(35) Cardenas, A. E.; Shrestha, R.; Webb, L. J.; Elber, R. Membrane Permeation of a Peptide: It Is Better to be Positive. *J. Phys. Chem. B* **2015**, *119*, 6412−6420.
(36) Sun, D.; Forsman, J.; Woodward, C. E. Evaluating force fields for the computational prediction of ionized arginine and lysine side-chains partitioning into lipid bilayers and octanol. *J. Chem. Theory Comput.* **2015**, *11*, 1775−1791.
(37) Berger, O.; Edholm, O.; Jähnig, F. Molecular dynamics simulations of a fluid bilayer of dipalmitoylphosphatidylcholine at full hydration, constant pressure, and constant temperature. *Biophys. J.* **1997**, *72*, 2002−2013.
(38) Bai, L.; Breen, D. Calculating center of mass in an unbounded 2D environment. *Journal of Graphics, GPU, and Game Tools* **2008**, *13*, 53−60.
(39) Leitold, C.; Dellago, C. Nucleation and structural growth of cluster crystals. *J. Chem. Phys.* **2016**, *145*, 074504.
(40) Pronk, S.; Páll, S.; Schulz, R.; Larsson, P.; Bjelkmar, P.; Apostolov, R.; Shirts, M. R.; Smith, J. C.; Kasson, P. M.; van der Spoel, D.; et al. GROMACS 4.5: a high-throughput and highly parallel open source molecular simulation toolkit. *Bioinformatics* **2013**, *29*, 845−854.
(41) Knight, C. J.; Hub, J. S. MemGen: A general web server for the setup of lipid membrane simulation systems. *Bioinformatics* **2015**, *31*, 2897−2899.
(42) Berendsen, H. J. C.; Postma, J. P. M.; van Gunsteren, W. F.; Hermans, J. In *Intermolecular Forces*; Pullman, B., Ed.; D. Reidel Publishing Company: Dordrecht, the Netherlands, 1981; pp 331−342.
(43) Miyamoto, S.; Kollman, P. A. SETTLE: An Analytical Version of the SHAKE and RATTLE Algorithms for Rigid Water Models. *J. Comput. Chem.* **1992**, *13*, 952−962.
(44) Hess, B. P-LINCS: A Parallel Linear Constraint Solver for Molecular Simulation. *J. Chem. Theory Comput.* **2008**, *4*, 116−122.
(45) van Gunsteren, W. F.; Berendsen, H. J. C. A Leap-Frog Algorithm for Stochastic Dynamics. *Mol. Simul.* **1988**, *1*, 173−185.
(46) Berendsen, H. J. C.; Postma, J. P. M.; van Gunsteren, W. F.; DiNola, A.; Haak, J. R. Molecular dynamics with coupling to an external bath. *J. Chem. Phys.* **1984**, *81*, 3684−3690.
(47) Darden, T.; York, D.; Pedersen, L. Particle mesh Ewald: an N·log(N) method for Ewald sums in large systems. *J. Chem. Phys.* **1993**, *98*, 10089−10092.
(48) Essmann, U.; Perera, L.; Berkowitz, M. L.; Darden, T.; Lee, H.; Pedersen, L. G. A smooth particle mesh ewald potential. *J. Chem. Phys.* **1995**, *103*, 8577−8592.
(49) Jämbeck, J. P. M.; Lyubartsev, A. P. Derivation and Systematic Validation of a Refined All-Atom Force Field for Phosphatidylcholine Lipids. *J. Phys. Chem. B* **2012**, *116*, 3164−3179.
(50) Jorgensen, W. L.; Chandrasekhar, J.; Madura, J. D.; Impey, R. W.; Klein, M. L. Comparison of simple potential functions for simulating liquid water. *J. Chem. Phys.* **1983**, *79*, 926−935.
(51) Pastor, R.; MacKerell, A., Jr Development of the CHARMM force field for lipids. *J. Phys. Chem. Lett.* **2011**, *2*, 1526−1532.
(52) Torrie, G. M.; Valleau, J. P. Monte Carlo free energy estimates using non-Boltzmann sampling: Application to the sub-critical Lennard-Jones fluid. *Chem. Phys. Lett.* **1974**, *28*, 578−581.
(53) Kumar, S.; Bouzida, D.; Swendsen, R. H.; Kollman, P. A.; Rosenberg, J. M. The weighted histogram analysis method for free-energy calculations on biomolecules. I. The method. *J. Comput. Chem.* **1992**, *13*, 1011−1021.
(54) Hub, J. S.; de Groot, B. L.; van der Spoel, D. g_wham−A Free Weighted Histogram Analysis Implementation Including Robust Error and Autocorrelation Estimates. *J. Chem. Theory Comput.* **2010**, *6*, 3713−3720.
(55) Bennett, W. D.; Tieleman, D. P. The Importance of Membrane Defects Lessons from Simulations. *Acc. Chem. Res.* **2014**, *47*, 2244−2251.
(56) Bennett, W. D.; Hong, C. K.; Wang, Y.; Tieleman, D. P. Antimicrobial Peptide Simulations and the Influence of Force Field on the Free Energy for Pore Formation in Lipid Bilayers. *J. Chem. Theory Comput.* **2016**, *12*, 4524−4533.
(57) Wennberg, C. L.; Murtola, T.; Hess, B.; Lindahl, E. Lennard-Jones lattice summation in bilayer simulations has critical effects on surface tension and lipid properties. *J. Chem. Theory Comput.* **2013**, *9*, 3527−3537.

DOI: 10.1021/acs.jctc.7b00106
J. Chem. Theory Comput. 2017, 13, 2352−2366